Cerebral Cortex December 2006;16:1701-1708
doi:10.1093/cercor/bhj105
Advance Access publication January 4, 2006

Differential Regional Atrophy of the Cingulate Gyrus in Alzheimer Disease: A Volumetric MRI Study

Bethany F. Jones[1], Josephine Barnes[2], Harry B.M. Uylings[3,4], Nick C. Fox[2], Chris Frost[2,5], Menno P. Witter[3] and Philip Scheltens[1]

[1]Department of Neurology, VU University Medical Centre, Amsterdam, The Netherlands, [2]Dementia Research Centre, Institute of Neurology, University College London, Queen Square, London, UK, [3]Department of Anatomy, VU University Medical Centre, Amsterdam, The Netherlands, [4]Netherlands Institute for Brain Research, KNAW, Amsterdam, The Netherlands and [5]Medical Statistics Unit, London School of Hygiene and Tropical Medicine, Keppel Street, London, UK

Magnetic resonance imaging–based volumetric measurements provide a useful technique for quantifying in vivo regional cerebral atrophy in Alzheimer disease (AD). Histopathological studies have shown the cingulate cortex, a cytoarchitectonically heterogeneous region, to be severely affected in AD. In this study, we developed and validated a manual segmentation protocol, based on macroscopic characteristics such as gyri and sulci patterns, in order to assess volumetric changes in 4 cingulate regions of interest. Cingulate cortical volumes of 10 familial AD patients were compared with 10 age- and sex-matched controls. Inter- and intrarater reliability coefficients were high for all cingulate regions (91.9–99.4%). All 4 cingulate regions were significantly smaller ($P < 0.05$) in AD cases compared with controls: rostral anterior cingulate gyrus (22.5% smaller), caudal anterior cingulate gyrus (20.7% smaller), posterior cingulate gyrus (44.1% smaller), and retrosplenial cortex (21.5% smaller). The atrophy in the posterior cingulate region was significantly greater than that in other cingulate regions ($P < 0.001$), suggesting a higher vulnerability for this region in familial AD. Considering the functional and connectional differences of these 4 cingulate regions, detection and monitoring of their atrophy may provide insights into the natural history of AD and may help in the search for diagnostic markers for early AD.

Keywords: anterior cingulate cortex, dementia, posterior cingulate cortex, retrosplenial cortex, volumetry

Introduction

Magnetic resonance imaging (MRI)–based volumetric measurements have proved to be useful for quantifying regional cerebral atrophy occurring in Alzheimer disease (AD) (Fox and others 2001). Postmortem studies have demonstrated that the atrophy in AD is associated with its defining histopathological changes, that is, the accumulation of neurofibrillary tangles and amyloid plaques, accompanied by widespread neuronal and synaptic loss (Braak H and Braak E 1991; Gomez-Isla and others 1996; Delacourte and others 1999; Rohn and others 2001; Uylings and de Brabander 2002). The implication therefore is that the macroscopic changes of progressive regional and global atrophy are a closely linked consequence of the underlying pathological processes in AD.

The hippocampus and entorhinal cortex are thought to be among the earliest sites of pathological involvement in AD (Braak H and Braak E 1991), and many volumetric MRI studies have focused on these regions in sporadic and familial AD, confirming their early involvement in vivo (Fox and others 1996; Jack and others 1999; Schott and others 2003). More recently, volumetric, functional, and neuropathological studies have also highlighted another area of the brain that appears to be involved from the very earliest stages of the disease: the cingulate cortex (Braak H and Braak E 1993; Minoshima and others 1997; Killiany and others 2000; Baron and others 2001; Callen and others 2001; Fox and others 2001; Frisoni and others 2002; Scahill and others 2002).

The cingulate cortex is a structurally and functionally heterogeneous region, located on the medial surface of the brain. It can be subdivided into an anterior cingulate (ACC) and a posterior cingulate (PCC) cortex (Vogt and others 1979; Baleydier and Mauguiere 1980). The PCC is subdivided further into the ventromedially located retrosplenial cortex (RS) and the more dorsally located PCC "proper" (Vogt and others 2001). The RS has particularly dense connections with the medial temporal lobe and demonstrates neurofibrillary changes at an earlier histopathological stage of AD compared with the rest of the PCC (Insausti and others 1987; Braak H and Braak E 1993; Suzuki and Amaral 1994; Lavenex and others 2002; Kobayashi and Amaral 2003). In view of these connectional and neuropathologic differences, cingulate subregions may differ with respect to their amount and rate of atrophy in AD. Methods to assess regional cingulate atrophy on MRI accurately may therefore provide insights into how the disease progresses and might ultimately be used to improve the diagnostic accuracy in very early stages of the disease (Kelly and others 1997; Baron and others 2001; Chetelat and Baron 2003).

Previous imaging studies have demonstrated atrophy in the PCC in AD. However, these studies either used different criteria to delineate and subdivide the cingulate cortex and did not subdivide the PCC (Killiany and others 2000; Callen and others 2001) or used semiautomatic techniques (Baron and others 2001; Fox and others 2001; Frisoni and others 2002; Scahill and others 2002), which may lack anatomic specificity for relatively small structures such as the RS (Ashburner and Friston 2000; Tisserand and others 2002; Crum and others 2003). Several studies have demonstrated atrophy in the ACC in later stages of the disease, but this was variably located in its rostral (Frisoni and others 2002; Scahill and others 2002) or its more caudal parts (Killiany and others 2000; Callen and others 2001).

The aim of the present study was to develop and validate a delineation protocol suitable for measuring atrophy of the different regions of the cingulate gyrus and subsequently to examine the regional pattern of cingulate atrophy in AD. For this purpose we compared the volumes of the different cingulate regions of interest (ROIs) in early-onset familial AD patients with those of age- and sex-matched control subjects. We studied early-onset familial AD patients because the diagnosis of AD can be made with relative certainty owing to their

known genetic risk. Moreover, in these patients comorbidity, such as vascular disease, is less of a confound. We also wanted to assess whether this protocol could reproducibly detect cortical volume reduction in smaller regions of the cingulate gyrus such as the RS.

Materials and Methods

Subjects

Ten subjects with familial AD, fulfilling criteria for probable AD (McKhann and others 1984) and 10 healthy age- and sex-matched controls recruited from the spouses of patients and healthy volunteers were selected for this study. Eight patients had genetic testing that confirmed mutations known to be pathogenic for AD (6 in amyloid precursor protein; 2 in presenilin-1), and 2 patients came from autosomal dominant pedigrees with pathology in a first degree relative. Subject demographics are described in Table 1. Subjects were assessed at the Dementia Research Centre at The National Hospital for Neurology and Neurosurgery in London and underwent annual MRI, Mini-Mental State Examination (MMSE) (Folstein and others 1975), and detailed clinical and neuropsychological assessment as part of an ongoing longitudinal research project. Subjects had no medical history of cerebrovascular or other chronic neurological disease, systemic disorders, or major psychiatric illnesses. The study was approved by the Local Research Ethics Committee, and all subjects had given written informed consent.

Magnetic Resonance Imaging Acquisition

T_1-weighted volumetric MR brain scans were acquired on a 1.5 Tesla Sigma unit (General Electric, Milwaukee, WI), using a spoiled gradient–echo technique (matrix: 256 × 128 × 128; acquisition parameters: time repetition/echo time/excitation, 35/5/1; flip angle, 35°). The scans were acquired as 124 contiguous 1.5-mm coronal slices and were transferred to a Sun workstation (Sun Microsystems Inc., Mountain View, CA) for analysis.

Image Analysis

Prior to segmentation, all scans were globally registered to the MNI 305 template using a 6 degrees of freedom registration algorithm (Mazziotta and others 1995). This ensured that all scans were measured in a similar orientation to improve consistency of segmentation.

The software package MIDAS (Freeborough and others 1997) was used for all manual segmentation. This tool allows simultaneous image viewing and outlining of regions in axial, coronal, and sagittal orientations. In order to prevent potential laterality bias, each image was presented twice in random order: once normally and once flipped across the midsagittal line. Delineation was always performed on the same side of the presented image. Measurements were performed by raters who were blind to the clinical diagnosis.

Cingulate borders were established using a combination of intensity thresholding and manual tracing using a mouse-driven cursor. A threshold setting between 70–110% of the mean brain intensity of the whole brain was used to give consistent delineation of cortical gray matter from cerebrospinal fluid and white matter. Whole-brain segmentation was performed using a previously described technique (Schott and others 2003). All regional cingulate boundaries were manually outlined and edited on the computer monitor.

Table 1
Subject demographics

	Controls	AD patients
Number	10	10
Sex F/M	5/5	6/4
Mean age (SD), years	51.0 (8.0)	51.8 (7.4)
MMSE score/30		
Mean (SD)	29.9 (0.4)	10.6 (6.2)
Range	29–30	5–21

Cingulate Borders

The cingulate gyrus largely comprises Brodmann areas 24, 23, 29, 30, and part of 31, and effort was taken to confine the analysis to these regions as much as possible. The rules that were applied for delineation of cingulate boundaries and subdivisions were based on cytoarchitectonic, connectional, and macroscopic studies (Ono and others 1990; Vogt and others 1995, 2001; Groenewegen and Uylings 2000; Uylings and others 2000; Tisserand and others 2002; Sanz-Arigita *et al* 2003; Vogt BA and Vogt LJ 2003). We will indicate in a step-by-step procedure how the macroscopic MRI delineations of ROIs can be roughly compared with microscopically defined Brodmann areas. It is essential to emphasize explicitly that macroscopic features like sulci often do not coincide precisely with cytoarchitectonic borders (Zilles 2004; Uylings and others 2005).

Sulcal Patterns and Variability

Figure 1 illustrates the gyri and sulci used to demarcate cingulate gyrus borders. The cingulate gyrus (CG) arches around the corpus callosum on the medial surface of the brain and is separated from this structure by the callosal sulcus (cas) (Fig. 1*A*). The cingulate sulcus (cs) forms the border between the cingulate gyrus and the anterodorsally located paracingulate gyrus (PCG) (Paus and others 1996; Tisserand and others 2002) and the (pre)motor cortex (MC) (Fig. 1*A*). The paracingulate gyrus may be heavily segmented (Fig. 1*A*) or more continuous (Fig. 1*B*) and may share a common origin with the cingulate gyrus (Fig. 1*C*). Rostral parts of the cingulate gyrus often contain a shallow secondary sulcus, running parallel to the cingulate sulcus (Ono and others 1990) (Fig. 1*A,B*, white arrowheads). Even in these cases the cingulate gyrus was always easy to distinguish from the anterodorsally located paracingulate gyrus. The cingulate sulcus continues up until the appearance of the marginal ramus (mr), from whence it continues as the splenial sulcus (sps) (Vogt and others 1995; termed subparietal sulcus by Ono and others 1990) (Fig. 1*A*). The splenial sulcus is highly variable in its pattern and often contains extensions directed towards the corpus callosum, which were included in the analysis (Fig. 1*B,C*, black arrowheads). The cingulate sulcus and splenial sulcus were sometimes interrupted, and in such cases the shortest possible line between the interrupted segments of the sulcus was drawn (see for e.g. Fig. 1*G*, curved arrow).

Demarcation of Cingulate Boundaries

As the cingulate gyrus curves around the anterior part of the corpus callosum a transition takes place from Brodmann area 24 to 25. In accordance with Tisserand and others (2002), the most caudal coronal slice on which the inner curvature of the genu of corpus callosum was visible was taken as the ventral–posterior border between areas 24 and 25 (Fig. 1*B*). In this manner area 25 was approximately excluded from the analysis. Area 25 is a more simple cortical structure than 24 (Vogt and others 1995, 2004). Posteriorly, the cingulate gyrus curves around the splenium of the corpus callosum where it ventrally borders the parahippocampal cortex. The most ventral axial slice on which the curvature of the splenium of the corpus callosum was visible has been taken as the macroscopic ventral border of the cingulate gyrus with the parahippocampal cortex because no cingulate cortex is present below this edge (Vogt and others 2001) (Fig. 1*B*).

Cingulate areas located dorsal to the corpus callosum were delineated on coronal slices (Fig. 1*D*), whereas cingulate areas located anterior and posterior to the corpus callosum were delineated on axial slices (Fig. 1*E,F*), respectively. On the right side of Figure 1*D–F* the cortical gray matter has been automatically delineated from CSF and white matter using a threshold setting between 70–110% of the mean brain intensity of the whole brain (MIDAS). On the left side of the figures the cingulate gyrus has been delineated. Cingulate gyrus borders were always set between the ventral and dorsal banks of the callosal sulcus and the cingulate sulcus (Sanz-Arigita and others 2003). The gray matter of the splenial sulcus was not included in the analysis (Fig. 1*F*). The splenial sulcus is surrounded by Brodmann area 31 (Vogt and others 2001). Effort was taken to exclude the major part of area 31 because it is also located on the parasplenial lobules posterodorsal to the cingulate gyrus (Vogt and others 2001), which was not a ROI (illustrated on sagittal sections in Fig. 1*G,H*). However, a small part of area 31 is located

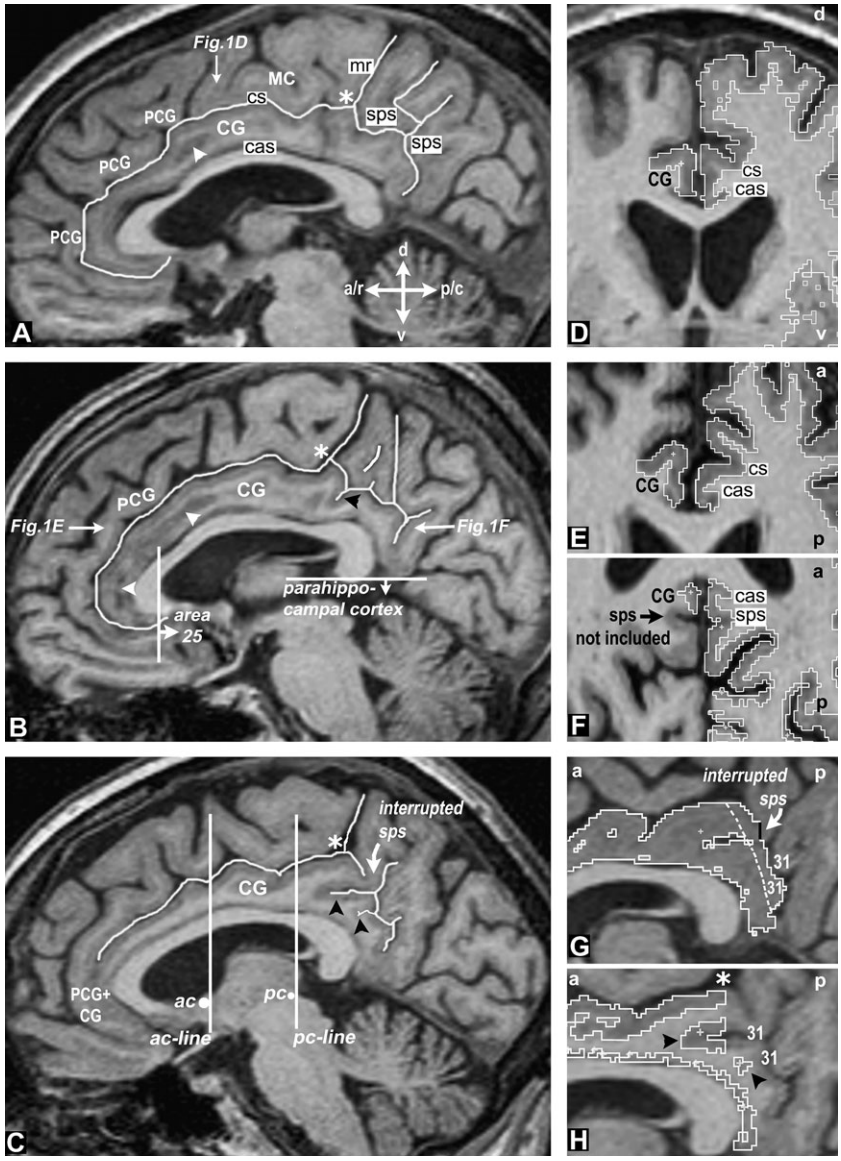

Figure 1. (*A–C*) Sagittal sections of MRI scans of 3 representative brains indicating the sulci, gyri, and reference points used to demarcate cingulate gyrus borders. (*D*) Coronal, (*E*, *F*) axial, and (*G*, *H*) sagittal sections, demonstrating cingulate gyrus borders within the relevant sulci. The asterisk indicates the site where the cingulate sulcus, splenial sulcus, and marginal ramus meet. Ac-line and pc-line in *C*: cutoff sections through the posterior edge of the anterior commissure (ac) and the posterior edge of the posterior commissure (pc) respectively, used for subdividing the cingulate gyrus. a/r = anterior/rostral; cas = callosal sulcus; CG = cingulate gyrus; cs = cingulate sulcus; d = dorsal; MC = (pre)motor cortex; mr = marginal ramus; p/c = posterior/caudal; PCG = paracingulate sulcus; sps = splenial sulcus; v = ventral: 31 = Brodmann area 31.

on the medial surface of the cingulate gyrus and cannot be delineated macroscopically (Fig. 1*G*, approximate border indicated by dotted line). Figure 1*G* is a more medial section of the brain in Figure 1*C*. In order to improve consistency, the entire medial surface of the cingulate gyrus was included in the analysis and thus also included a small part of area 31. The gray matter located within the splenial sulcus was removed in sagittal slices (Fig. 1*H*). Note that in Figure 1*H* extensions of the splenial sulcus directed towards the corpus callosum were included in the analysis (black arrowheads).

Cingulate ROI Subdivisions

The most caudal coronal slice on which the anterior commisure (ac) was visible (Fig. 1*C*, ac-line) and the most caudal coronal slice on which the posterior commisure was visible (Fig. 1*C*, pc-line) were used to subdivide the cingulate gyrus. The orientation of the coronal slices in our scans corresponds with the ac- and pc-line in Figure 1*C*. The resulting subdivision of the cingulate gyrus and its borders within the sulci, together with the approximate location of the relevant Brodmann areas, is indicated in Figure 2. Anterior parts of the cingulate gyrus were subdivided into a rostral ROI (termed rostral AC, located anterior to the ac-line) and a caudal ROI (termed caudal AC, located between the ac- and pc-line) (Fig. 2*A–C*). Although both ACC regions approximately correspond to Brodmann area 24, more recent studies have demonstrated a number of cytological and functional differences between them justifying a subdivision (Vogt BA and Vogt LJ 2003; Vogt and others 2003). Although the cingulate and paracingulate gyrus share a common origin in this specific brain, a slight indentation is visible in the medial part of the gray matter, which was taken as the border between these regions (Fig. 2*B*, arrow). The posterior region of the cingulate gyrus (located caudal to the pc-line) was divided into a PCC ROI (termed PC) and the RS (Fig. 2*A,D,E*). The border between the PC and the RS is the only border that can be objectively delineated macroscopically (Vogt and others 2001). The RS corresponds with Brodmann areas 29 and 30 and is located in the depth of the callosal sulcus and does not appear on the medial surface of the cingulate gyrus, which comprises area 23

(Fig. 2*D,E*). Thus, when manually indicating the border of the RS (black line in Fig. 2*D,E*) care was taken not to include any medially located pixels.

Reproducibility

In order to assess intra- and interrater reproducibility, regional cingulate volumes of 10 patients (20 hemispheres) were each measured twice by 2 different raters (B.F.J. and J.B.). Subdivisions of the posterior cingulate gyrus (PC, RS) were measured twice by one rater (B.F.J.), in order to assess the feasibility of separating these 2 regions in the further analysis. Reproducibility for the whole cingulate gyrus and component parts was assessed by calculating within-subject standard deviations (SDs) and reliability coefficients (RCs) (Bartko 1966; Fleis 1986).

Statistical Analysis

Statistical analysis were conducted using the statistical package STATA versions 6 and 8 (Stata, College Station, TX) and Microsoft Excel 2000. In order to normalize scans for individual differences in head size, the total intracranial volume (TIV) was calculated from T_1-weighted scans using a previously described semiautomated technique (Whitwell and others 2001). The logs of the mean cingulate ROI volumes of the control group were regressed against the logs of the mean TIV measures to establish the slope of the relationship between TIV and cingulate volume. The resulting coefficient (α) was used to correct the cingulate volumes as follows:

$$b_i^* = b_i(t_0/t_i)^{\alpha},$$

where b_i^* is the adjusted cingulate volume, b_i the crude cingulate volume, t_i the TIV for the ith individual, and t_0 the mean TIV.

Differences in volumes between 1) AD cases and controls, 2) cingulate ROIs, and 3) left and right sides were assessed using a random effects generalized least squares regression model. All volumes were log-transformed (to allow estimation of percentage differences), and 2-way interaction terms were included to investigate the extent to which 1) the difference between AD cases and controls differed between regions, 2) the left–right difference differed between regions, and 3) the left–right difference differed between AD cases and controls. Pairwise contrasts were used to investigate interactions where a global interaction test was statistically significant.

Results

Reproducibility

Reproducibility, expressed in terms of RCs and SDs as percentages are given in Table 2. Intra- and interrater RCs were

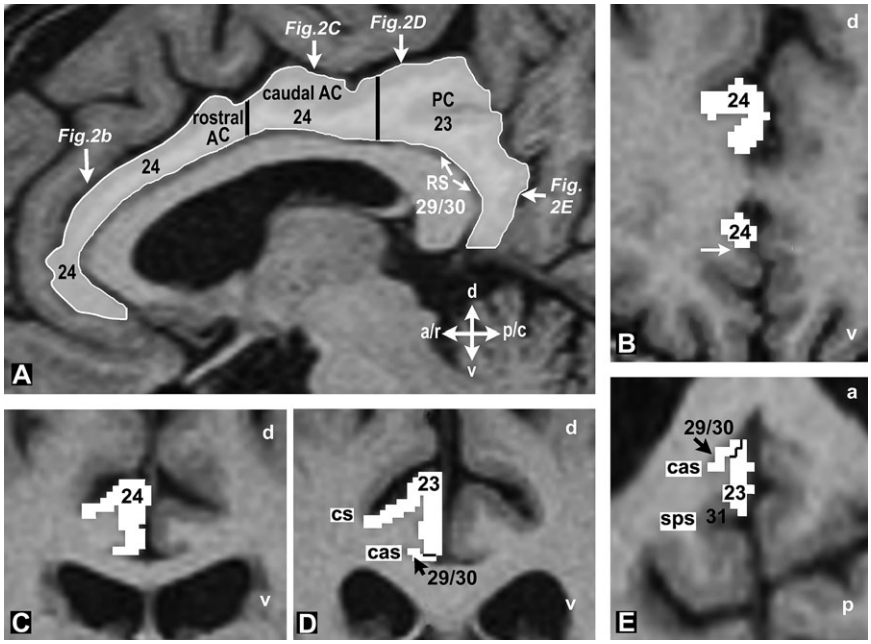

Figure 2. (*A*) Sagittal, (*B–D*) coronal, and (*E*) axial views of the same MRI scan illustrating the location of the cingulate subdivisions together with approximate corresponding Brodmann areas. (*A*) The orientation and location of the sections in 2*B–E* have been indicated. (*B*, *C*) Coronal sections through the rostral and caudal AC respectively. (*D*) Coronal and (*E*) axial section through the PC and RS. Abbreviations are the same as in Figure 1.

Table 2
Intrarater and interrater reproducibility for the whole cingulate gyrus and subdivisions expressed as RCs and SDs

	Intrarater reproducibility				Interrater reproducibility			
	Left		Right		Left		Right	
	RC (%)	SD (%)	RC (%)	SD (%)	RC (%)	SD (%)	RC (%)	SD (%)
Whole cingulate	99.4	2.4	98.5	2.8	97.9	4.1	99.1	2.2
Rostral AC	97.8	5.6	99.1	2.7	93.5	9.3	99.2	2.5
Caudal AC	97.9	3.9	97.8	3.8	98.8	2.8	98.4	3.2
PC + RS	96.2	7.9	98.5	4.4	94.9	9.2	98.9	3.8
PC	94.4	10.4	98.3	5.1	[a]	[a]	[a]	[a]
RS	91.9	9.1	92.4	8.3	[a]	[a]	[a]	[a]

Note: All variables have been log-transformed to facilitate expression of within-subject SDs as percentages.
[a]Performed by one rater.

comparable and ranged from 91.4–99.4%. Considering the high reproducibility for the PC and the RS (>91.9%; Donner and Eliasziw 1987), these 2 regions were fitted separately into the statistical model and not pooled together.

Cingulate ROI Volumes

The TIV-corrected cingulate ROI volumes for both groups are shown in Figure 3.

There was statistically significant evidence of a group by region interaction (i.e., that the magnitude of the difference between AD cases and controls differed between regions combining over hemispheres) (P = 0.0025), a hemisphere by region interaction (P = 0.034), but no evidence of a group by hemisphere interaction (i.e., no evidence that the case–control difference differed between the left and right side combining over regions) (P = 0.8). Accordingly, the 2-way interaction between group and hemisphere was dropped from the model effectively pooling the differences between AD cases and controls over left and right sides. All the cingulate ROIs were significantly smaller in cases compared with controls with the difference in the PC being significantly larger than that in each

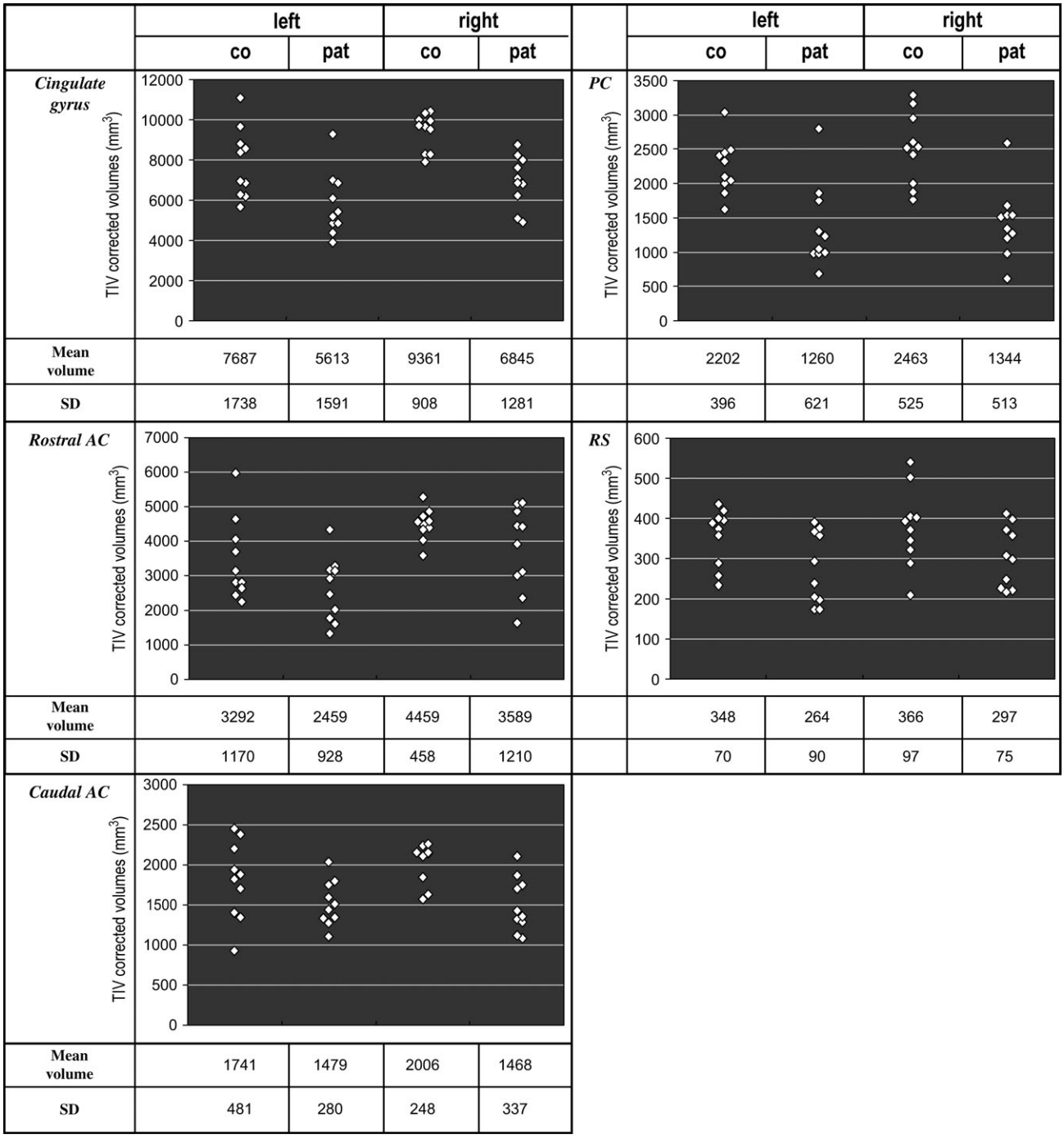

Figure 3. Volumetric differences between AD patients (n = 10) and controls (n = 10). Mean volumes are displayed as TIV-corrected geometric mean volumes.

of the other cingulate regions ($P < 0.01$): rostral AC: 22.5% (95% confidence interval [CI] 6.2–35.9%) smaller, $P = 0.009$; caudal AC: 20.7% (95% CI 4.1–34.4%) smaller, $P = 0.017$; PC: 44.1% (95% CI 32.4–54.8%) smaller, $P < 0.001$; RS: 21.5% (95% CI 5.1–35.1%) smaller, $P = 0.012$ (Fig. 3).

On average, cingulate volumes were larger on the right side in all regions in both AD cases and controls, with some evidence ($P = 0.034$) that the magnitude of the left–right difference varies between regions. This left–right difference was greatest for the rostral AC, and this was the only region where the difference was statistically significant.

Despite the fact that mean volumes for all 4 cingulate ROIs differed significantly between cases and controls, Figure 3 shows that there was considerable overlap, which was least in the PCC ROI. We calculated sensitivity and specificity values for the PC in order to determine how well these data might classify individuals into their diagnostic groups. With a cutoff value of 1880 mm^3 for the mean of the left and right PC, the sensitivity was 90%, specificity 100%, positive predictive value 100%, and the negative predictive value was 91%.

The wide range of MMSEs in the patient group raises the possibility that the results are driven by the very severe cases. To investigate this, Pearson correlation coefficients between MMSE scores and cingulate volumes were calculated. None of the volumes of the cingulate ROIs showed a correlation with MMSE scores that was statistically significant or large enough to support such a hypothesis: rostral AC $r = -0.36$ ($P = 0.38$); caudal AC $r = -0.35$ ($P = 0.39$); PC $r = -0.23$ ($P = 0.59$); RS $r = 0.04$ ($P = 0.93$).

Discussion

Using an MR-based manual delineation protocol for the cingulate gyrus we have demonstrated that all 4 cingulate ROIs (rostral AC, caudal AC, PC, RS) show a significant atrophy in familial AD patients compared with controls. Within the cingulate gyrus, the volume reduction was the greatest in the PC ROI. Our analysis detected previously described left–right hemisphere asymmetries in cingulate volumes (right > left), which accords with other studies (Paus and others 1996; Watkins and others 2001). The severity of the volume loss did not differ between left and right cingulate regions in the AD subjects.

A potential source of variability in region-based manual outlining results from difficulty in accurately correlating cytoarchitectonic borders in histological sections with gross anatomical landmarks on MR scans in vivo. Often the macroscopic sulci do not coincide with borders of microscopically cytoarchitectonically defined cortical areas (Zilles 2004; Uylings and others 2005). A high degree of interindividual variability in sulcal patterns, as is the case with the cingulate gyrus, further adds to this problem (Vogt and others 1995; Paus and others 1996). Although manual demarcation of brain regions is time consuming, it is still the gold standard of ROI measurement on MRI (Tisserand and others 2002; Crum and others 2003). Our manual demarcation protocol was standardized as much as possible and yielded high inter- and intrarater RCs, ranging from 91.9–99.4%. The landmarks selected to define the borders of the cingulate gyrus and its subdivisions in the present study were based on extensive examination of morphological and cytoarchitectonic studies, and the analyzed cingulate subregions approximate to Brodmann areas 24 (rostral + caudal AC), 29 + 30 (RS), and 23 (PC).

Separate evaluation of these regions in AD may be relevant taking into account the fact that neurofibrillary tangles in the RS are present in relatively early neuropathological stages of AD and precede pathological changes in areas 23 and 24 (Braak H and Braak E 1993). These tangles are not present in healthy controls and therefore may represent preclinical stages of AD (Ma and others 1994). Furthermore, in nonhuman primates, rostral area 24 and the RS have dense reciprocal connections with the entorhinal and (para)hippocampal cortex, whereas caudal areas 24 and 23 do not (Insausti and others 1987; Suzuki and Amaral 1994; Lavenex and others 2002; Kobayashi and Amaral 2003). Considering the differences in medial temporal lobe connections and temporal patterns of neuropathological involvement, it interesting that not the RS but the PC ROI ($\approx$ area 23) showed the greatest volumetric loss in the present study. The apparent selective vulnerability of area 23 in AD cannot be explained as secondary to deafferentiation as a result of medial temporal lobe damage. Rather, this selective volume loss seems to be related to neurodegeneration because a number of neuropathological studies have demonstrated severe neuron losses in area 23 in those cases with clinically established symptoms of AD (Vogt and others 1990, 1998).

The PC ROI is capable of separating subjects from controls with a high sensitivity (90%) and specificity (100%). Measurements of medial temporal lobe measures have found similar levels of sensitivity and specificity (Scheltens and others 1992; Juottonen and others 1999; Killiany and others 2002). Although the number of subjects in the present study is small, this region seems promising as a diagnostic indicator of AD.

Previous macroscopic MRI studies have demonstrated PC cortex atrophy in AD patients using semiautomated techniques (Baron and others 2001; Frisoni and others 2002; Scahill and others 2002). According to these authors, the atrophy appeared to predominate around the splenial sulcus, including the dorsal part of the posterior cingulate gyrus and did not seem to involve retrosplenial areas, which partially corresponds with our findings. Atrophy of the rostral (but not the caudal) AC was not evident until later stages of the disease (Frisoni and others 2002; Scahill and others 2002). Automated methods require spatial normalization and smoothing techniques and are probably less suitable for analyzing highly variable cortical regions (AC) or small areas (e.g., RS) (Ashburner and Friston 2000; Crum and others 2003). A manual ROI study has shown significant atrophy of the caudal AC and the PC in AD but did not reveal any significant atrophy in the rostral AC. However, this study included the paracingulate gyrus in the AC and did not subdivide the posterior cingulate gyrus and thus did not assess the RS separately (Callen and others 2001).

In the present study we have described and validated a manual delineation protocol to measure atrophy of 4 different cingulate regions on MRI. The present study is the first to find significant atrophy of all 4 cingulate regions in AD. We have also shown that our delineation protocol is capable of detecting atrophy in smaller regions of the cingulate gyrus, such as the RS. To our knowledge, this study is the first to assess the volumes of the PCC and the RS separately. Considering the connectional and functional heterogeneity of these areas, regional cingulate atrophy measures may aid in understanding the way in which the disease begins and progresses and may also help in the search for diagnostic markers of early AD.

Notes

We gratefully acknowledge Medical Research Council (UK) support. Traveling fees for this study were provided by the Alzheimer Centre of the VU University Medical Centre in Amsterdam, the Netherlands. Furthermore, the authors would like to thank Ernesto Sanz-Arigita for his kind help in defining ACC borders on MRI scans.

Address correspondence to Bethany F. Jones, Department of Neurology, VU University Medical Center, Postbus 7057, 1007 MB Amsterdam, The Netherlands. Email: b.jones@vumc.nl.

References

Ashburner J, Friston KJ. 2000. Voxel-based morphometry—the methods. Neuroimage 11:805–821.

Baleydier C, Mauguiere F. 1980. The duality of the cingulate gyrus in monkey. Neuroanatomical study and functional hypothesis. Brain 103:525–554.

Baron JC, Chetelat G, Desgranges B, Perchey G, Landeau B, de la Sayette V, Eustache F. 2001. In vivo mapping of gray matter loss with voxel-based morphometry in mild Alzheimer's disease. Neuroimage 14:298–309.

Bartko JJ. 1966. The intraclass correlation coefficient as a measure of reliability. Psychol Rep 19:3–11.

Braak H, Braak E. 1991. Neuropathological stageing of Alzheimer-related changes. Acta Neuropathol (Berl) 82:239–259.

Braak H, Braak E. 1993. Alzheimer neuropathology and limbic circuits. In: Vogt BA, Gabriel M, editors. Neurobiology of cingulate cortex and limbic thalamus: a comprehensive handbook. Boston, MA: Birkhauser. p 606–627.

Callen DJ, Black SE, Gao F, Caldwell CB, Szalai JP. 2001. Beyond the hippocampus: MRI volumetry confirms widespread limbic atrophy in AD. Neurology 57:1669–1674.

Chetelat G, Baron JC. 2003. Early diagnosis of Alzheimer's disease: contribution of structural neuroimaging. Neuroimage 18:525–541.

Crum WR, Griffin LD, Hill DLG, Hawkes DJ. 2003. Zen and the art of medical image registration: correspondence, homology, and quality. Neuroimage 20:1425–1437.

Delacourte A, David JP, Sergeant N, Buee L, Wattez A, Vermersch P, Ghozali F, Fallet-Bianco C, Pasquier F, Lebert F, Petit H, Di Menza C. 1999. The biochemical pathway of neurofibrillary degeneration in aging and Alzheimer's disease. Neurology 52:1158–1165.

Donner A, Eliasziw M. 1987. Sample size requirements for reliability studies. Stat Med 6:441–448.

Fleis JL. 1986. Design and analysis of clinical experiments. New York: Wiley-Interscience.

Folstein MF, Folstein SE, McHugh PR. 1975. "Mini-mental state." A practical method for grading the cognitive state of patients for the clinician. J Psychiatr Res 12:189–198.

Fox NC, Crum WR, Scahill RI, Stevens JM, Janssen JC, Rossor MN. 2001. Imaging of onset and progression of Alzheimer's disease with voxel-compression mapping of serial magnetic resonance images. Lancet 358:201–205.

Fox NC, Freeborough PA, Rossor MN. 1996. Visualisation and quantification of rates of atrophy in Alzheimer's disease. Lancet 348:94–97.

Freeborough PA, Fox NC, Kitney RI. 1997. Interactive algorithms for the segmentation and quantitation of 3-D MRI brain scans. Comput Methods Programs Biomed 53:15–25.

Frisoni GB, Testa C, Zorzan A, Sabattoli F, Beltramello A, Soininen H, Laakso MP. 2002. Detection of grey matter loss in mild Alzheimer's disease with voxel based morphometry. J Neurol Neurosurg Psychiatry 73:657–664.

Gomez-Isla T, Price, JL, McKeel DW, Morris JC, Growdon JH, Hyman BT. 1996. Profound loss of layer II entorhinal cortex neurons occurs in very mild Alzheimer's disease. J Neurosci 16:4491–4500.

Groenewegen HJ, Uylings HBM. 2000. The prefrontal cortex and the integration of sensory, limbic and autonomic information. Prog Brain Res 126:3–28.

Insausti R, Amaral DG, Cowan WM. 1987. The entorhinal cortex of the monkey: II. Cortical afferents. J Comp Neurol 264:356–395.

Jack CR, Petersen RC, Xu YC, O'Brien PC, Smith GE, Ivnik RJ, Boeve BF, Waring SC, Tangalos EG, Kokmen E. 1999. Prediction of AD with MRI-based hippocampal volume in mild cognitive impairment. Neurology 52:1397–1403.

Juottonen K, Laakso MP, Partanen K, Soininen H. 1999. Comparative MR analysis of the entorhinal cortex and hippocampus in diagnosing Alzheimer disease. Am J Neuroradiol 20:139–144

Kelly CA, Harvey RJ, Cayton H. 1997. Drug treatments for Alzheimer's disease. Br Med J 314:693–694.

Killiany RJ, Gomez-Isla T, Moss M, Kikinis R, Sandor T, Jolesz F, Tanzi R, Jones K, Hyman BT, Albert MS. 2000. Use of structural magnetic resonance imaging to predict who will get Alzheimer's disease. Ann Neurol 47:430–439.

Killiany RJ, Hyman BT, Gomez-Isla T, Moss MB, Kikinis R, Jolesz F, Tanzi R, Jones K, Albert MS. 2002. MRI measures of entorhinal cortex vs hippocampus in preclinical AD. Neurology 58:1188–1196.

Kobayashi Y, Amaral DG. 2003. Macaque monkey retrosplenial cortex: II. Cortical afferents. J Comp Neurol 466:48–79.

Lavenex P, Suzuki WA, Amaral DG. 2002. Perirhinal and parahippocampal cortices of the macaque monkey: projections to the neocortex. J Comp Neurol 447:394–420.

Ma C, Wang G, Braak H. 1994. Pathological changes in the retrosplenial cortex in senile dementia of the Alzheimer type. Chin Med J 107:119–123.

Mazziotta JC, Toga AW, Evans A, Fox P, Lancaster J. 1995. A probabilistic atlas of the human brain: theory and rationale for its development. The International Consortium for Brain Mapping (ICBM). Neuroimage 2:89–101.

McKhann G, Drachman D, Folstein M, Katzman R, Price D, Stadlan EM. 1984. Clinical diagnosis of Alzheimer's disease: report of the NINCDS-ADRDA Work Group under the auspices of Department of Health and Human Services Task Force on Alzheimer's Disease. Neurology 34:939–944.

Minoshima S, Giordani B, Berent S, Frey KA, Foster NL, Kuhl DE. 1997. Metabolic reduction in the posterior cingulate cortex in very early Alzheimer's disease. Ann Neurol 42:85–94.

Ono M, Kubic S, Abernathey CD. 1990. Atlas of the cerebral sulci. Stuttgart: Thieme Medical Publishers.

Paus T, Tomaiuolo F, Otaky N, MacDonald D, Petrides M, Atlas J, Morris R, Evans AC. 1996. Human cingulate and paracingulate sulci: pattern, variability, asymmetry, and probabalistic map. Cereb Cortex 6:207–214.

Rohn TT, Head E, Su JH, Anderson AJ, Bahr BA, Cotman CW, Cribbs DH. 2001. Correlation between caspase activation and neurofibrillary tangle formation in Alzheimer's disease. Am J Pathol 158:189–198.

Sanz-Arigita EJ, De Vos K, Pool CW, Zilles K, Uylings HBM. 2003. Individual variability of human anterior cingulate cortex combined with 3D MRI. Neuroimage 19:S20.

Scahill RI, Schott JM, Steven JM, Rossor MN, Fox NC. 2002. Mapping the evolution of regional atrophy in Alzheimer's disease: unbiased analysis of fluid-registered serial MRI. Proc Natl Acad Sci USA 99:4703–4707.

Scheltens P, Leys D, Barkhof F, Huglo D, Weinstein HC, Vermersch P, Kuiper M, Steinling M, Wolters EC, Valk J. 1992. Atrophy of medial temporal lobes on MRI in "probable" Alzheimer's disease and normal ageing: diagnostic value and neuropsychological correlates. J Neurol Neurosurg Psychiatry 55:967–972.

Schott JM, Fox NC, Frost C, Scahill RI, Janssen JC, Chan D, Jenkins R, Rossor MN. 2003. Assessing the onset of structural change in familial Alzheimer's disease. Ann Neurol 53:181–188.

Suzuki WA, Amaral DG. 1994. Perirhinal and parahippocampal cortices of the macaque monkey: cortical afferents. J Comp Neurol 350:497–533.

Tisserand DJ, Pruessner JC, Sanz-Arigita EJ, van Boxtel MP, Evans AC, Jolles J, Uylings HBM. 2002. Regional frontal cortical volumes decrease differentially in aging: an MRI study to compare volumetric approaches and voxel-based morphometry. Neuroimage 17:657–669.

Uylings HBM, de Brabander JM. 2002. Neuronal changes in normal human aging and Alzheimer's disease. Brain Cogn 49:268–276.

Uylings HBM, Rajkowska G, Sanz Arigita E, Amunts K, Zilles K. 2005. Consequences of large interindividual variability for human brain atlases: converging macroscopical imaging and microscopical neuroanatomy. Anat Embryol 210:423–431.

Uylings HBM, Sanz-Arigita EJ, de Vos K, Smeets WJ, Pool CW, Amunts K, Rajkowska G, Zilles K. 2000. The importance of a human 3D database

and atlas for studies of prefrontal and thalamic functions. Prog Brain Res. 126:357–368.
Vogt BA, Berger GR, Derbyshire SW. 2003. Structural and functional dichotomy of human midcingulate cortex. Eur J Neurosci 18:3134–3144.
Vogt BA, Hof PR, Vogt LJ. 2004. Cingulate gyrus. In: Paxinos G, Mai JK, editors. The human nervous system. San Diego, CA: Academic Press. p 915–949.
Vogt BA, Nimchinsky EA, Vogt LJ, Hof PR. 1995. Human cingulate cortex: surface features, flat maps, and cytoarchitecture. J Comp Neurol 359:490–506.
Vogt BA, Rosene DL, Pandya DN. 1979. Thalamic and cortical afferents differentiate anterior from posterior cingulate cortex in the monkey. Science 204:205–207.
Vogt BA, Van Hoesen GW, Vogt LJ. 1990. Laminar distribution of neuron degeneration in posterior cingulate cortex in Alzheimer's disease. Acta Neuropathol 80:581–589.
Vogt BA, Vogt LJ. 2003. Cytology of human dorsal midcingulate and supplementary motor cortices. J Chem Neuroanat 26:301–309.
Vogt BA, Vogt LJ, Perl DP, Hof PR. 2001. Cytology of human caudomedial cingulate, retrosplenial, and caudal parahippocampal cortices. J Comp Neurol 438:353–376.
Vogt BA, Vogt LJ, Vrana KE, Gioia L, Meadows RS, Challa VR, Hof PR, Van Hoesen GW. 1998. Multivariate analysis of laminar patterns of neurodegeneration in posterior cingulate cortex in Alzheimer's disease. Exp Neurol 153:8–22.
Watkins KE, Paus T, Lerch JP, Zijdenbos A, Collins DL, Neelin P, Taylor J, Worsley KJ, Evans AC. 2001. Structural asymmetries in the human brain: a voxel-based statistical analysis of 142 MRI scans. Cereb Cortex 11:868–877.
Whitwell JL, Crum WR, Watt HC, Fox NC. 2001. Normalization of cerebral volumes by use of intracranial volume: implications for longitudinal quantitative MR imaging. Am J Neuroradiol 22: 1483–1489.
Zilles K. 2004. Architecture of the human cerebral cortex. Regional and laminar organization. In: Paxinos G, Mai JK, editors. The human nervous system. San Diego, CA: Academic Press. p 997–1055.